Confined-interface-directed synthesis of Palladium single-atom catalysts on graphene/amorphous carbon

Jiangbo Xi[a,b], Hongyu Sun[c], Da Wang[d], Zheye Zhang[a], Xianming Duan[a], Junwu Xiao[a], Fei Xiao[a], Limin Liu[d,**], Shuai Wang[a,*]

[a] *Key laboratory of Material Chemistry for Energy Conversion and Storage, Ministry of Education, School of Chemistry and Chemical Engineering, Huazhong University of Science and Technology, Wuhan, 430074, PR China*
[b] *School of Chemistry and Environmental Engineering, Wuhan Institute of Technology, Wuhan, 430205, PR China*
[c] *Department of Micro- and Nanotechnology, Technical University of Denmark, 2800 Kongens Lyngby, Denmark*
[d] *Beijing Computational Science Research Center, Beijing 100193, PR China*

ARTICLE INFO

ABSTRACT

The maximized atomic efficiency of supported catalysts is highly desired in heterogeneous catalysis. Therefore, the design and development of active, stable, and atomic metal-based catalysts remains a formidable challenge. To tackle these problems, it is necessary to investigate the interaction between single atoms and supports. Theoretical calculations indicate that the Pd binding strength is higher on graphene/amorphous carbon (AC) than that on graphene or AC substrate. Based on these predictions, we present a facile confined-interface-directed synthesis route for the preparation of single-atom catalysts (SACs) in which Pd atoms are well-dispersed on the interface of double-shelled hollow carbon nanospheres with reduced graphene oxide (RGO) as the inner shell and AC as the outer shell. Owing to the synergetic effect of the RGO/AC confined interface and the atomically dispersed Pd, the as-made RGO@AC/Pd SAC achieves the maximum atomic efficiency (catalytic activity) of Pd species and exhibits an excellent stability in chemical catalysis. This confined-interface-directed synthesis method provides a novel direction to maximize the atomic efficiency, improve the activity, and enhance the stability of metal-based catalysts.

1. Introduction

Supported noble metal catalysts are widely used in industry owing to their high activity and/or selectivity for many key chemical reactions [1]. However, industrial catalysts base on precious metal suffer from several drawbacks, including scarcity and the resulting high cost as well as poor stability and recyclability. Consequently, extensive research efforts have focused on strategies for increasing the active sites, either by reducing the size of catalyst clusters [2] or by producing particles with externally exposed high index facets [3]. Downsizing noble metals to ultrafine clusters or even single atoms has recently emerged as a new research frontier [4]. In this way, full atom utility can be obtained from the lowest size limit in a catalyst. Thus, metals are usually finely divided into nanometer-sized particles [5], subnanometer-sized clusters [6] or even single atoms [7] and dispersed onto high-surface-area support to maximize the metals' atomic efficiency and achieve the desired catalytic performance [8]. Despite the effectiveness of this strategy, the size reduction often generates unsaturated coordination

sites on the metal species that enhances activity but makes them structurally unstable [9]. Consequently, dispersed metal clusters or single atoms require optimized anchoring to mitigate unfavorable aggregation or coarsening during the catalytic process owing to their increased surface free energy [4]. As is known, the interaction between single atoms and supported catalysts is crucial to stabilizing these active single atoms [2]. As a result, much effort has been focused on this strategy by embedding the downsized single atoms into supported catalysts, which have shown excellent catalytic performance [2,10]. However, a clear understanding of the formation mechanism and of the maximized atomic efficiency of single-atom catalysts (SACs) is still lacking. Therefore, the design and development of active, stable, and atomic metal-based catalysts remains a formidable challenge. To tackle these problems, it is necessary to investigate the interaction between single atoms and supports.

Carbon materials, such as amorphous carbon (AC) and graphene have been widely used to disperse metal particles for advanced supported catalysts [11–14]. Nevertheless, the processes involved in

---

* Corresponding author at: School of Chemistry and Chemical Engineering, Huazhong University of Science and Technology, Wuhan, 430074, PR China.
** Corresponding author.
E-mail addresses: limin.liu@csrc.ac.cn (L. Liu), chmsamuel@mail.hust.edu.cn (S. Wang).

anchoring single metal atoms on carbon materials have not been intensively investigated. To design and prepare novel carbon supported SACs, density functional theory (DFT) calculations were conducted to investigate the interaction between single atoms and carbonaceous supports. According to our calculation results, Pd atoms are prone to adsorption and deposition on the confined interface between graphene and AC and preferentially separate from each other. Inspired by the theoretical predictions, we designed and fabricated a new type of Pd-based SAC by a reduced graphene oxide@AC (RGO@AC) confined-interface-directed synthesis method. This atomically dispersed Pd catalyst was constructed with a double-shelled hollow carbon nanosphere (HCN) of RGO@AC with Pd single atoms loaded onto its confined interface, and this catalyst exhibited extremely high activity and stability for 4-nitrophenol (4-NP) reduction and the Suzuki coupling reaction.

2. Experimental section

2.1. Computational methods

The computations were performed through Tianhe-2JK at the Beijing Computational Science Research Center (CSRC). Our calculations were performed with DFT, as implemented in the Vienna ab initio package (VASP) [15]. The general gradient approximation of Perdew-Burke-Ernzerhof (GGA-PBE) was adopted for the exchange-correlation functional [16]. Moreover, the electron-wave functions were expanded by a plane-wave cutoff of 400 eV. The $(4 \times 4 \times 1)$ supercell RGO with a stoichiometry of C_{50} was constructed by the periodic boundary condition (PBC), and the vacuum layers were set to be larger than 20 Å to avoid periodic interaction. The initial structure of the amorphous carbon (AC) structure studied here was obtained from a previous study with bulk a-C with a density of 3.0 g/cm^3 [17]. A two-dimensional slab of a-C was obtained by removing the periodicity in the z direction (surface normal direction) using a supercell of dimensions $12.5 \times 12.5 \times 20.0$ Å^3 instead of the bulk a-C supercell of $12.5 \times 12.5 \times 5.4$ Å^3. The dangling bonds at the bottom of the slab were terminated with 23 pseudo-hydrogen atoms, yielding an initial surface structure with a total of 163 atoms (128C and 23 H-terminations). The strategy of using the pseudo-hydrogen atoms to saturate the dangling bonds to maintain the bulk coordination environment has also been widely used in the studies of metal, metal oxide and carbon-based catalysis [18–20]. The reciprocal space was performed by the Monkhorst-Pack special k-point scheme with $2 \times 2 \times 1$ grid meshes for structural relaxation for the AC slab. Atomic relaxation was performed until the total energy variation was smaller than 10^{-6} eV and all forces on each atom were less than 0.01 eV/Å.

The ab initio molecular dynamics (AIMD) simulations were performed using the CP2 K/QUICKSTEP package [21]. The wave functions of the valence electrons were expanded in terms of Gaussian functions with molecularly optimized double-ζ polarized basis sets (m-DZVP), which ensures a small basis set superposition error [22], and core electrons were described with norm-conserving Goedecker, Teter, and

Hutter (GTH) pseudo potentials [23]. The AIMD simulations were conducted with the NVT ensemble at a target temperature along with a Nose-Hoover thermostat (Fig. S1). A simple cubic lattice was chosen as the initial configuration of the atoms, as this structure is highly unstable for carbon. Once molten, the sample was equilibrated at 5000 K for 0.36 ps, where the liquid was highly diffusive with a diffusion constant of 7×10^{-5} cm^2/s. The liquid sample was then cooled to 300 K over 0.5 ps; following this, the system was equilibrated for a further 0.5 ps to gain temporal averages. The cooling rate of 10^{16} K/s is similar to that used in other simulations of carbon [24,25].

2.2. The detailed fabrication process of the RGO@AC/Pd atomic catalyst

#### 2.2.1. Synthesis of GO-wrapped SiO_2 (SiO_2@GO) spheres

SiO_2 spheres (100–200 nm) were synthesized as templates by the Stöber method [26]. GO was prepared according to a modified Hummers method [27]. In a typical synthesis, 0.2 g of SiO_2 spheres was first dispersed in 100 mL of ethanol by sonication for 20 min. Next, 1 mL of 3-aminopropyltrimethoxysilane was added and refluxed for 5 h to obtain amine-functionalized SiO_2 nanospheres. After the products were centrifuged and redispersed in 100 mL of DI water, 30 mL of 0.2 mg/mL GO aqueous solution was added and stirred vigorously for 1 h. During this process, the amino-functionalized SiO_2 nanospheres were tightly wrapped by GO nanosheets through electrostatic interactions and hydrogen bonds between the amino groups and the oxygen-containing groups on the GO sheets (step 1 in Fig. S4) [28]. Finally, the products were collected by centrifugation, washed with water several times, and then dried at 60 °C overnight.

#### 2.2.2. Synthesis of double-shelled hollow carbon spheres (RGO@AC)

The surface of the SiO_2@GO nanospheres was further coated by AC precursor layers via the pyrolysis of glucose under hydrothermal conditions and a subsequent thermal treatment procedure (step 2 in Fig. S4), accompanying the thermal reduction of GO to RGO [29]. Typically, 150 mg of as-prepared SiO_2@RGO spheres were dispersed in 16 mL of a water/ethanol (volume ratio = 3/1) mixture by ultrasonication. Then, 4 mL of 0.5 M aqueous glucose solution was added under vigorous stirring for 30 min. After that, the suspension was transferred to a 25 mL Teflon-lined autoclave and heated in an oven at 180 °C for 16 h. The dark gray products were collected by centrifugation and washed with ethanol and DI water six times. After drying at 60 °C overnight, the resulting dark gray powder was carbonized at 900 °C for 4 h under an inert atmosphere. Finally, the as-prepared SiO_2@RGO@AC spheres were then transformed into RGO@AC HCNs by etching the SiO_2 cores with HF solution ($\approx 2\%$) twice (step 3 in Fig. 1).

2.2.3. Synthesis of double-shelled hollow carbon spheres with the pd catalyst (RGO@AC/Pd)

RGO@AC composites (50 mg) were dispersed in 50 mL of DI water. Then, 0.5 mg of K_2PdCl_4 were added to the suspension and stirred vigorously for 2 h in an ice bath. During this process, Pd atoms were
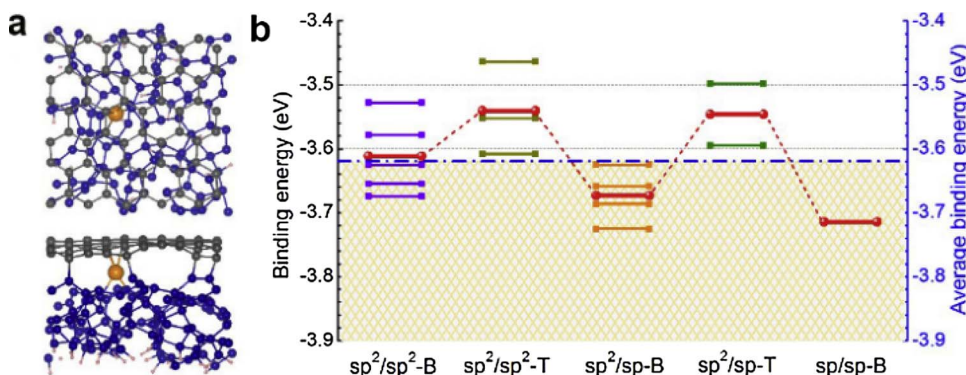
Fig. 1. (a) Top (above) and side (bottom) views of the representative sites for Pd intercalated in AC/graphene. The blue, gray, yellow and light red balls indicate C (AC), C (graphene), Pd and H, respectively. (b) Binding energies of the Pd atom intercalated in 16 different positions. The average binding energies of five different types of adsorption structures are shown in red, and the blue dashed line indicates the total average binding energy of the AC/Pd/graphene system. (For interpretation of the references to colour in this figure legend, the reader is referred to the web version of this article.)
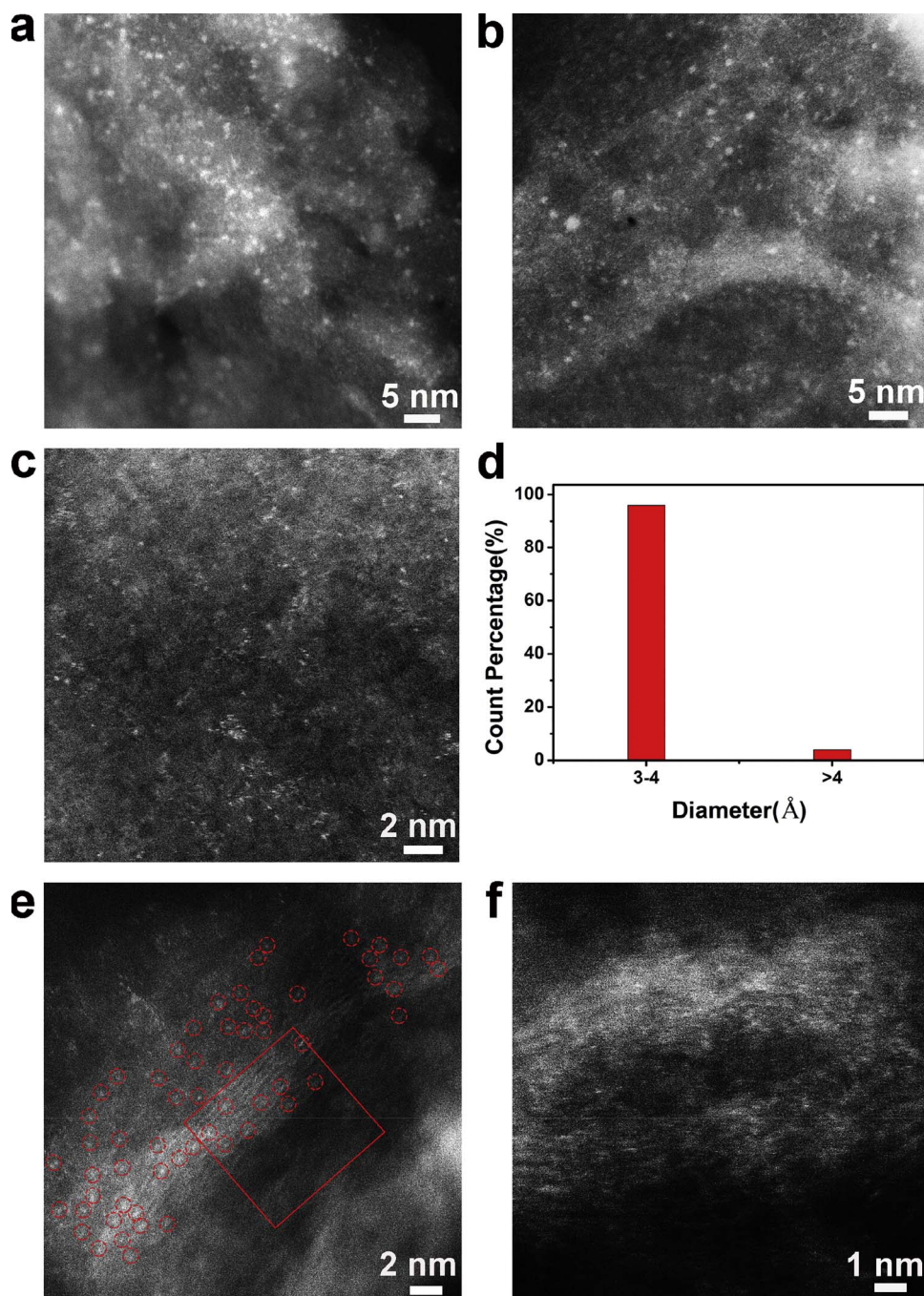
Fig. 2. (a) AC-STEM image of the interface for the AC/Pd and (b) RGO/Pd composites; (c) AC-STEM image of the RGO@AC/Pd HCNs, revealing a high density of Pd atoms (bright dots in red circles); (d) the corresponding size distribution of the bright spots in Fig. 2c; (e) AC-STEM image of the RGO@AC/Pd HCNs and (f) enlarged AC-STEM image of Fig. 2e, which reveals that the Pd atoms are embedded in the thin shell of the RGO@AC HCNs. (For interpretation of the references to colour in this figure legend, the reader is referred to the web version of this article.)

deposited on the support by a facile and green method via the adsorption of $PdCl_4^{2-}$ directed to the confined interface of the RGO@AC HCNs, leading to the formation of the atomically dispersed RGO@AC/Pd catalyst (step 4 in Fig. S4). Afterwards, the reaction mixture was filtered and washed three times with pure water to remove the remaining reagents.

3. Results and discussion

3.1. DFT results

We first examined the adsorption properties of single Pd atoms in an AC/graphene structure by DFT calculations. For comparison, the adsorption strengths of Pd atoms on AC and graphene were also calculated. The structural properties of the constructed AC film are in good agreement with experiments (Supplementary Information, Fig. S1 and Table S1), particularly with regard to the nearest neighbor distances r_1 and r_2 at a density of 3.0 g/cm^3. In the AC film, the sp^3 concentration remains the same as in the bulk. However, some of the former bulk sp^2 atoms convert to sp coordination on the surface (Table S1), which has also been indicated in previous theoretical work [30]. As Pd atoms adsorbed on the AC surface (Supplementary Information, Fig. S2a), a total of 21 different configurations were obtained, where carbon atoms with sp^3 hybridization are mostly located deeper within the surface and have an extremely low activity for Pd adsorption due to full occupation of the C-s/p orbitals. As a result, the average binding strength for the interactions of Pd atoms with C of sp^3-, sp^2- and sp-hybridization was calculated to be -3.28 eV. In addition, as Pd adsorbed on the graphene side, bridge sites (Pd_B) were found to be more stable than other sites (Pd_T), the corresponding binding energies were calculated to be
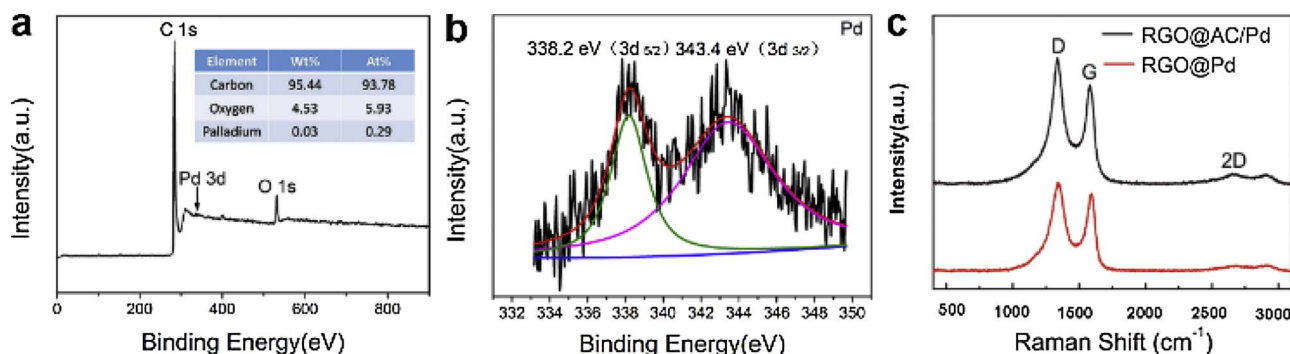
Fig. 3. (a) XPS survey spectrum of the RGO@AC/Pd composite (inset is the elemental analysis). (b) High-resolution XPS spectrum of Pd 3d. (c) Raman spectra of the RGO@AC/Pd and RGO/Pd catalysts.

−2.03 eV (Pd$_B$) and −1.76 eV (Pd$_T$).

Considering the Pd atoms adsorbed onto the AC/graphene structure (Fig. 1a), 16 different configurations were obtained, which can be divided into five types (Fig. 1b). We denote the Pd atom located on the AC and graphene layers as Pd(AC) and Pd(graphene), respectively, where Pd(AC) includes the sp^2/sp^2 sites, sp/sp sites and sp^2/sp sites, and Pd(graphene) contains the bridge and top sites. It is clearly shown in Fig. 1b that Pd atoms located at sp/sp (AC)-B (graphene) sites are energetically more stable than the other cases. More importantly, the total average binding energy of Pd atoms in AC/graphene (-3.62 eV) is larger than those of Pd in the most stable sites of graphene (-2.03 eV) and the AC system (-3.28 eV), indicating the enhancement of the binding strength in the constructed AC/graphene structure.

To further examine the distribution of Pd atoms in AC/graphene and their propensity to agglomerate, the energy difference, ΔE$_c$, between the isolated Pd configuration and a Pd cluster configuration was calculated [21]:

$$\Delta E_c = E(Pd_2AC \& G) + E(AC \& G) - E_1(Pd_1AC \& G) - E_2(Pd_1AC \& G)$$

In this equation, a larger the positive value of ΔE$_c$ indicates a stronger tendency for the Pd atoms to separate from each other. As shown in Supplementary Fig. S3, it is more favorable for the Pd atoms to separate from each other in AC/graphene. As the Pd–Pd distances are larger than 5.5 Å, there are almost no interactions between Pd atoms.

3.2. Morphology and characterization of RGO@AC/Pd catalysts

RGO@AC double-shelled HCNs were constructed by a templating method, with RGO as the inner shell and AC as the outer shell (Supplementary Information, Fig. S4, S5a, 5b and 5c). Then, well-dispersed Pd atoms were deposited on the confined interface of the RGO@AC HCNs by a facile impregnation method via a directed adsorption of Pd species, without using surfactants or capping reagents. For comparison, AC/Pd and RGO/Pd composites were also fabricated under the same conditions and used as control samples. A large number of Pd clusters were observed in aberration-corrected scanning transmission electron microscopy (AC-STEM) images for both the AC/Pd (0.7–3 nm, 0.312 wt.%) (Fig. 2a and Supplementary Information, Fig. S6) composite and the RGO/Pd composite (0.4–3 nm, 0.346 wt.%) (Fig. 2b and Supplementary Information, Fig. S7). Noticeably, no formation of nanosized Pd clusters was observed in the AC-STEM image (Supplementary Information, Fig. S5d and S8a) of the obtained RGO@AC/Pd catalyst. According to the corresponding high-angle annular dark-field (HAADF) images (Fig. 2c), several bright dots (in this case, Pd) with an average particle size of approximately 3–4 Å were well-dispersed in the RGO@AC HCNs, which matches the van der Waals diameter of a single Pd atom [31]. The size distribution in Fig. 2d reveals that the size of 96% of the Pd species in the RGO@AC HCNs is less than 4 Å, further demonstrating that most of the Pd exists as isolated single atoms. HAADF-STEM was conducted to probe the fine structure of the RGO@AC/Pd composites. As shown in Fig. 2e and f and Supplementary Fig. S8b, visible Pd atoms were mainly distributed on the middle region of RGO/AC shell rather than the outer surface, indicating that the atomic Pd was well-embedded on the confined interface of RGO@AC HCNs. These results are consistent with DFT calculations in which the total average binding energy of Pd atoms in graphene/AC was larger than that in the graphene or AC systems, indicating an enhancement of the binding strength in the graphene/AC structure. In addition, it was found that redox reaction may occur between carbonaceous species and metal ions due to the different potential levels between them, and thus leading to the spontaneous deposition of metal onto the carbon materials [32,33]. Therefore, it is reasonable to conclude that PdCl$_4^{2-}$ is prone to be induced and deposited on the confined interface between AC and RGO, leading to the formation of single confined Pd atoms. As a result, these experimental observations combined with the DFT calculations demonstrate the contribution of RGO/AC confined interface to the deposition of atomically dispersed Pd and thus provide a mechanism for the confined-interface-directed synthesis method.

The chemical compositions of the RGO@AC/Pd composite were further characterized by X-ray photoelectron spectroscopy (XPS). The XPS survey spectrum reveals the presence of C, O and Pd signals in the sample (Fig. 3a), which is consistent with the element composition of RGO@AC/Pd. The high-resolution spectrum of Pd 3d was deconvoluted into two single peaks at 338.2 eV and 343.4 eV (Fig. 3b), indicating the presence of Pd (II) in the RGO@AC/Pd sample [34,35]. In addition, the Pd content in the RGO@AC/Pd composite was as low as 0.290 wt.%, which is in good agreement with the value (0.292 wt.%) determined using a microwave plasma-atom emission spectrometer (MP-AES). Fig. 3c shows the Raman spectra of the RGO@AC/Pd and RGO/Pd catalysts. The intensity ratio of the 2D/G value of the RGO@AC/Pd catalyst (0.541) is much higher than that of the RGO/Pd (0.157) system. The 2D Raman peak is characteristic of single- and few-layer graphene, indicating that the outer carbon shells effectively prevent the collapsing of the hollow structure and thus prevent the π–π stacking of the inner RGO shells [36]. Furthermore, without the AC support, the spherical shell constructed by pristine RGO nanosheets collapses after removing the SiO$_2$ cores, causing a reduction of the 2D Raman peak intensity. This finding is in accordance with the TEM image shown in Supplementary Fig. S7, in which the RGO nanosheets in the RGO/Pd catalyst were restacked.

3.3. Catalytic performance of RGO@AC/Pd catalysts

To evaluate the catalytic activity, RGO@AC/Pd was used as a catalyst in the reduction of 4-NP to 4-aminophenol (4-AP) (Fig. 4a). Fig. 4b shows the UV–vis spectra changes of the reaction mixture in the presence of the RGO@AC/Pd catalyst. The absorption of 4-NP at 400 nm quickly disappeared, and the absorption of 4-AP at approximately
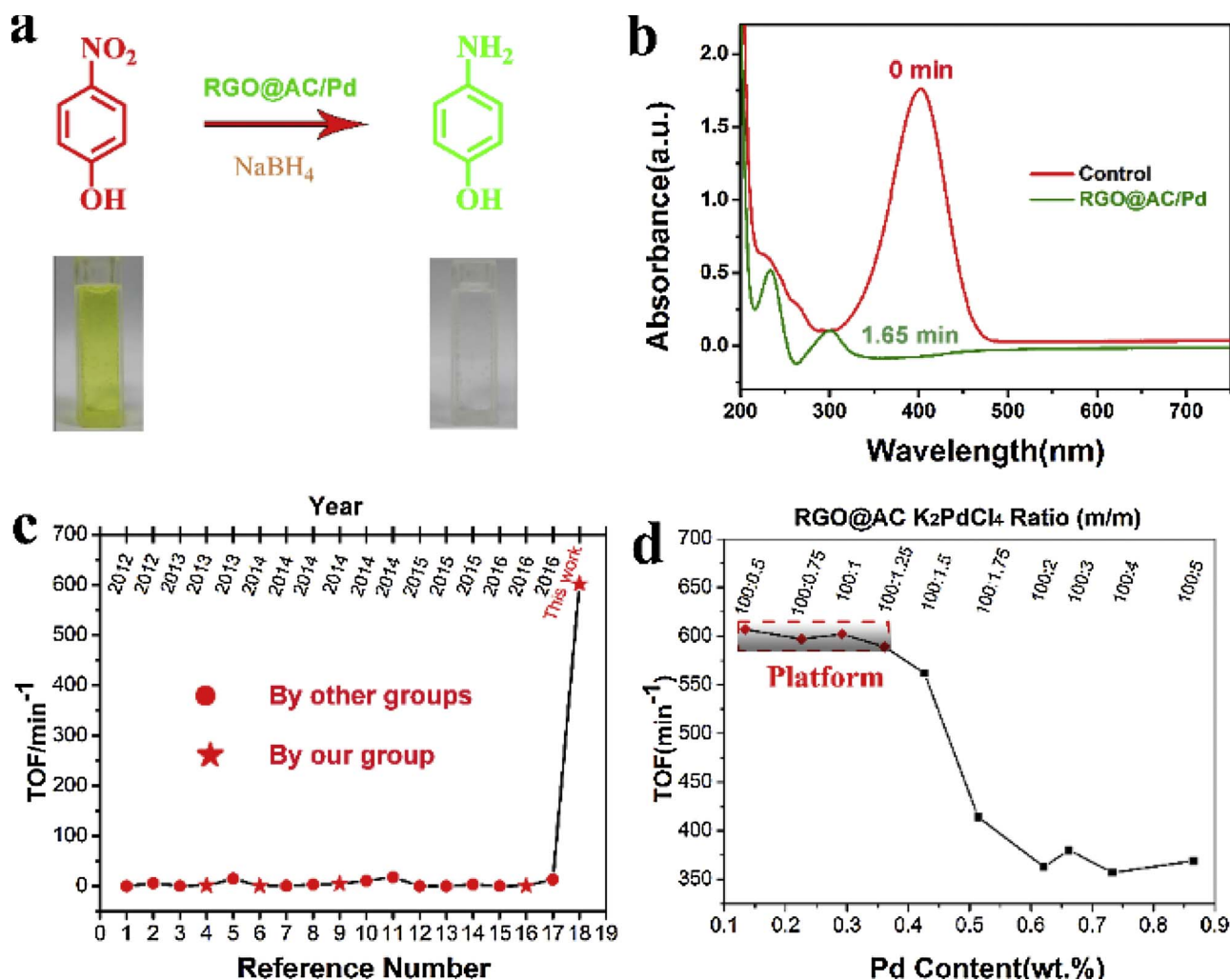
Fig. 4. (a) Reaction equation of 4-NP to 4-AP used in this work to evaluate the catalytic activity of the RGO@AC/Pd catalyst. The lower photographs show the color change from the conversion of 4-NP to 4-AP. (b) UV/vis spectra of the original 4-NP-NaBH₄ control solution (red) and the reduced 4-NP-NaBH₄ solution after adding the RGO@AC/Pd catalyst and reacting for 1.65 min (green). (c) Comparison of the TOFs in this work with those previously reported by our group and other groups. (d) TOFs of the RGO@AC/Pd catalysts with different Pd contents. (For interpretation of the references to colour in this figure legend, the reader is referred to the web version of this article.)

300 nm increased accordingly. In addition, the complete reduction of 4-NP to 4-AP was detected by a color change from bright yellow to colorless (the inset of Fig. 4a). Significantly, the reduction of 4-NP to 4-AP was complete within 1.65 min (99 s), even when the content of Pd was as low as 0.292 wt.%. The turnover frequency (TOF, defined here as the amount of reactant that 1 mmol of Pd converts into product per min) of the RGO@AC/Pd catalyst was as high as 602 min⁻¹, which is much higher than those of the RGO/Pd (106 min⁻¹) and AC/Pd (97 min⁻¹) catalysts even they have comparable Pd amount (0.312 wt.% for AC/Pd and 0.346 wt.% for RGO/Pd). Ideally for metal-based catalysts, metal particles should be well-dispersed as single atoms to expose all the catalytic sites, which are essential to achieve maximum atomic efficiency in catalysis. Given the much lower loading amount of metal in the catalysts, there need to be more available isolated active sites with higher atomic efficiency. In RGO@AC/Pd SAC, every isolated Pd atom can act as a single catalytic site and thus take full advantage of supported metal. Thereof, this extremely high performance of RGO@AC/Pd should be attributable to the unique properties of the SAC, which can maximize the efficiency of noble-metal atoms [37]. This TOF is higher than most other recently reported Pd/carbonaceous-support-based catalysts. As shown in Fig. 4c and Supplementary Table S2, this TOF exceeds those of conventional Pd/carbonaceous-support-based catalytic systems by a factor of more than 30.

Considering that Suzuki couplings (the subject of the 2010 Nobel Prize in Chemistry) are indispensable reactions for aryl–aryl bond formation in biaryl compounds [38], we further chose the Suzuki coupling reaction as a model reaction to estimate the catalytic activity of the RGO@AC/Pd SAC. Our results show that iodobenzene can be completely converted into biphenyl efficiently using the RGO@AC/Pd SAC (0.361 wt.%) as the catalyst. The TOF for the reaction was 280 min⁻¹, which is much higher than that of previously reported Pd-based catalysts (Supplementary Information, Table S3).

Catalysts with different metal contents were also investigated to obtain a better understanding of this confined-interface-directed synthesis method. The formation of Pd atoms, the sizes and location of the synthesized Pd clusters are easily tuned by altering the loading amount. Generally, increasing the Pd content leads to the gradual growth of Pd clusters. Interestingly, the size distribution of Pd atoms remains nearly intact when the Pd content is varied below 0.40 wt.% (e.g., 0.134 wt.%, 0.226 wt.%, 0.292 wt.% or 0.361 wt.%) (Supplementary Information, Fig. S8-11). It is noted that a minority of tiny Pd clusters were observed when the Pd content was increased to 0.426 wt.% (Supplementary Fig. S12). When the Pd content reached 0.621 wt.%, the size of the Pd clusters increased to approximately 1 nm (Supplementary Fig. S13). Notably, when the Pd content reached 1.662 wt.%, both Pd clusters and nanoparticles were observed on both the interface and outer/inner surfaces surface on the RGO@AC HCNs (Supplementary Fig. S14). This finding suggests that the Pd atoms are

preferentially adsorbed onto the graphene/AC-confined interface when the when the Pd content is lower than 0.40 wt.% due to strong anchoring effects. Furthermore, formation and location of Pd atoms or nano cluster are dependent on the ratio of RGO@AC and K_2PdCl_4 (m/m).

The superior catalytic performance of the atomic catalyst must originate from the well-dispersed Pd atoms confined in the interfaces of the RGO@AC HCNs, as the RGO@AC support itself is neither adsorptive nor catalytically active for the 4-NP reduction reaction (Supplementary Information, Fig. S15). The well-dispersed Pd single atoms provide highly dense active sites and thus increase the catalytic activity [7,31,39]. Notably, in the low catalyst loading regime, there is little change of the TOF value (ca. 600 min^{-1}) when these atomic catalysts have different Pd contents [0.134 wt.% (607 min^{-1}), 0.226 wt.% (597 min^{-1}), 0.292 wt.% (602 min^{-1}) and 0.361 wt.% (589 min^{-1})] (Fig. 4d). This constant high TOF value represents the maximized atomic efficiency of Pd, further confirming the existence of atomically dispersed Pd. As we increase the catalyst loading amount, the activity and atomic efficiency begin to decrease [0.426 wt.% (562 min^{-1}), 0.514 wt.% (414 min^{-1}), 0.621 wt.% (363 min^{-1}), 0.733 wt.% (357 min^{-1}) and 0.865 wt.% (369 min^{-1})]. This phenomenon can be attributed to the formation of Pd nanoclusters, leading to a lower atomic efficiency and TOF value [4,40], which was confirmed by TEM images (Supplementary Information, Fig. S9-14). On the other hand, the RGO@AC/Pd catalyst with large free reaction voids inside of the carbon sphere can provide more active sites that can act as a nanoreactor and offer a high substrate concentration near the Pd atoms, thus enhancing catalytic performance [41]. As shown by the micrograph in Supplementary Fig. S16, the obtained RGO@AC/Pd catalyst exhibits a hollow structure. Moreover, the RGO@AC/Pd catalyst possesses a thin shell (ca. 20 nm) and unique nanoporous structure on the double-shelled support, which leads to enhanced diffusion of the reactant and facile mass transportation, thus enhancing catalytic performance [42]. Furthermore, the RGO@AC support has a large specific surface area of 666.5 $m^2 g^{-1}$ (Supplementary Information, Fig. S17) and strong π-π interaction between the inner RGO shell and the benzene-containing reactants (4-NP), and leading to excellent exposure of active sites (Pd atoms) and easier access of the reactants to active sites. Based on the abovementioned results, a possible mechanism can be proposed to explain the enhanced performance of the SACs for this chemical catalysis process. The catalytic reduction may occur in three steps: (1) reducing agent ($NaBH_4$) react with the surface of the Pd atoms and transfer surface-hydrogen species to the surface of the Pd; (2) the reactant molecule (4-NP) diffused onto the carbonaceous support in solution and contact with the exposed active site, followed by the simultaneous reduction in the presence of reductive hydrogen species; and (3) finally, the product (4-AP) diffused away from the catalyst. The synergetic effect of the different components in the RGO@AC/Pd SAC and the confinement effect can greatly enhance catalytic activity. This confinement effect has also been observed in catalysis involving CNTs [43].

To evaluate the stability of the RGO@AC/Pd catalyst, repeated catalytic tests and electron beam irradiation tests were performed. The 4-NP conversion remained at a constant value (100%) without any decay during five repeated catalytic cycles and was only reduced to 95% after the 8th repeated cycle (Fig. 5a). This result suggests that essentially no aggregation of the Pd single atoms occurred, which was confirmed by the HAADF-STEM images (Fig. 5b). The size distribution in the inset of Fig. 5b reveals that 89% of the Pd species in the RGO@AC HCNs are atomically dispersed, further confirming the stability of the Pd atoms at the RGO@AC-confined interface. The HAADF-STEM images revealed that the Pd species exist exclusively as isolated single atoms in the RGO@AC HCNs after a 6 min electron beam irradiation test (Fig. 5c and 5d), further demonstrating the excellent stability of the RGO@AC/Pd catalyst. By comparison, Pd nanoparticles loaded onto the surface of the support (e.g., AC HCNs or RGO nanosheets) exhibited poor stability as indicated by repeated catalytic tests (Supplementary Information,

Fig. S18 and S19). These results further suggest that the Pd atoms were anchored in the confined interface rather than on the outer surface of the RGO@AC HCNs. According to the calculations, it is more favorable for Pd atoms to be isolated in AC/graphene than in the graphene or AC system. In addition, the calculated formation energies of the distributed Pd atoms in graphene/AC and the Pd–Pd clusters also show that there is nearly no interaction between the Pd atoms, which is supported by the Pd–Pd distance of greater than 5.5 Å. As a result, it is more favorable for the Pd single atoms anchored at the confined interface of RGO/AC to separate from each other, which is consistent with our experimental results. As elucidated above, these data combined with the theoretical simulations constitute reasonable explanations for the formation mechanism and stability of atomically dispersed Pd in the RGO@AC/Pd SACs.

4. Conclusion

In summary, we present a confined-interface-directed synthesis method for SACs based on DFT calculations of the interaction between single atoms and carbonaceous supports. This synthetic strategy allowed us to produce a well-controlled atomic catalyst in which atomically dispersed Pd formed inside of the confined interface between graphene and AC. Owing to the synergetic effect of the well-dispersed atomic Pd and the presence of the RGO/AC interface, the as-made RGO@AC/Pd SAC showed an ultrahigh activity and excellent stability for 4-NP reduction. By optimizing the loading amount of Pd in the RGO@AC/Pd SACs, we also achieved the maximum atomic efficiency of Pd in the 4-NP catalytic reduction. Furthermore, the RGO@AC/Pd SAC was also applied to the Suzuki coupling reaction and showed ultrahigh activity. We believe that these findings will motivate theoretical and experimental studies to advance the fundamental understanding of the interaction between different single atoms and other types of RGO/AC interfaces. It is anticipated that the confined-interface-directed synthesis approach can be applied for the preparation of extremely efficient and stable SACs, which can be used in a broad range of metal-catalyzed reactions.

Author contributions

S. W. and J. B. X. conceived the idea and co-wrote the manuscript. J. B. X., Z. Y. Z., X. M. D., F. X., and J. W. X carried out the materials synthesis and the chemical catalysis. L. M. L. and D.W. performed the DFT calculation. H. Y. S and J. B. X performed the materials characterizations. S. W. proposed, planned and supervised the project. All of the authors discussed the results and commented on the manuscript. The manuscript was written through contributions of all authors. All authors have given approval to the final version of the manuscript. J. B. X., H. Y. S., D.W. and Z. Y. Z. contributed equally.
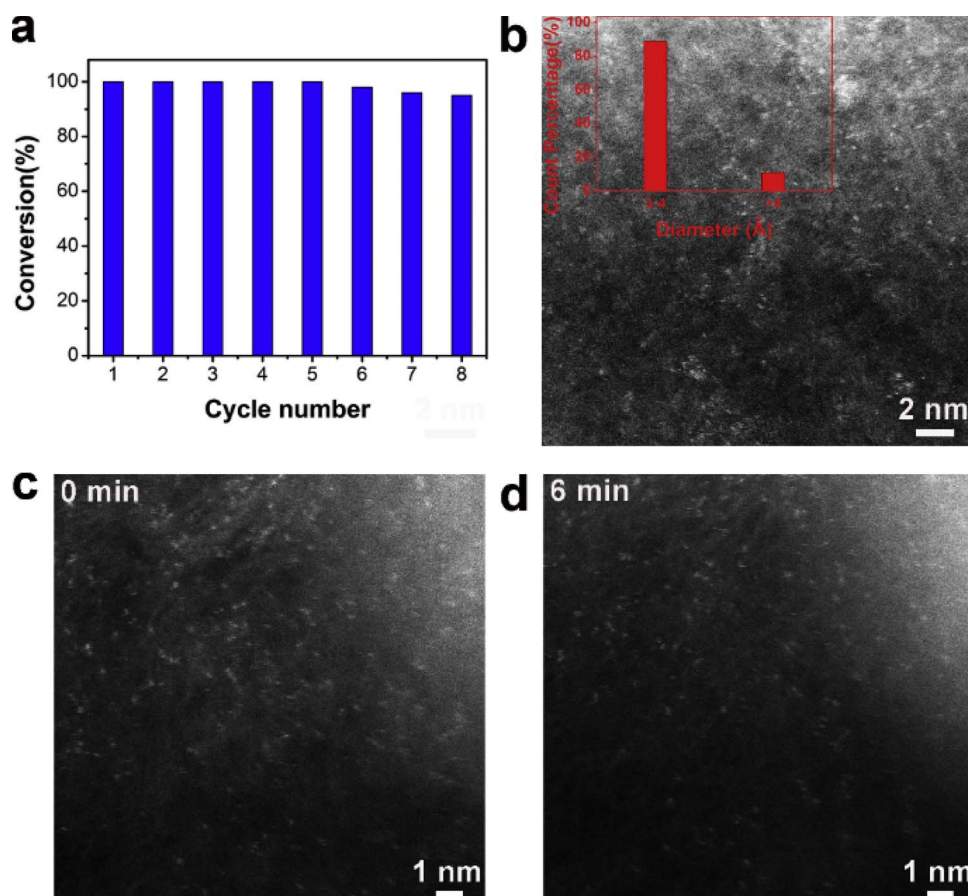
Conflict of interest

The authors declare no conflict of interest.

Acknowledgements

Fig. 5. (a) The stability of the catalysts shown by performing the same 4-NP reduction reaction over eight repeated cycles; (b) HAADF-STEM image of the RGO@AC/Pd catalyst after the repeated catalytic tests, showing that the catalyst is stable after reaction and that the Pd species remain atomically dispersed. The inset is the corresponding size distribution of the Pd species in Fig. 2b. HAADF-STEM images of the RGO@AC/Pd catalyst (c) before and (d) after electron beam irradiation tests. Taken together, the atomic dispersion of Pd is preserved during the 4-NP reduction measurements and electron beam irradiation tests.

Appendix A. Supplementary data

Supplementary data associated with this article can be found, in the online version, at https://doi.org/10.1016/j.apcatb.2017.11.057.

References

[1] B.T. Qiao, A.Q. Wang, X.F. Yang, F.A. Lawrence, Z. Jiang, Y.T. Cui, J.Y. Liu, J. Li, T. Zhang, Nat. Chem. 3 (2011) 634–641.
[2] X.G. Li, W.T. Bi, L. Zhang, S. Tao, W.S. Chu, Q. Zhang, Y. Luo, C.Z. Wu, Y. Xie, Adv. Mater. 28 (2016) 2427–2431.
[3] N. Tian, Z.Y. Zhou, S.G. Sun, Y. Ding, Z.L. Wang, Science 316 (2007) 732–735.
[4] X.F. Yang, A.Q. Wang, B.T. Qiao, J. Li, J.Y. Liu, T. Zhang, Acc. Chem. Res. 46 (2013) 1740–1748.
[5] J.B. Xi, C.Y. Xie, Y. Zhang, L. Wang, J. Xiao, X.M. Duan, J.H. Ren, F. Xiao, S. Wang, ACS Appl. Mater. Interfaces 8 (2016) 22563–22573.
[6] A.B. Redondo, M. Ranocchiari, J.A. van Bokhoven, Dalton Trans. 45 (2016) 2983–2988.
[7] P. Liu, Y. Zhao, R.X. Qin, S.G. Mo, G.X. Chen, L. Gu, D.M. Chevrier, P. Zhang, Q. Guo, D.D. Zhang, B.H. Wu, G. Fu, N.F. Zheng, Science 352 (2016) 797–800.
[8] A.T. Bell, Science 299 (2003) 1688–1691.
[9] R.H. Ouyang, J.X. Liu, W.X. Li, J. Am. Chem. Soc. 135 (2012) 1760–1771.
[10] X.F. Zhang, J.J. Guo, P.F. Guan, C.J. Liu, H. Huang, F.H. Xue, X.L. Dong, S.J. Pennycook, M.F. Chisholm, Nat. Commun 4 (2013) 1924.
[11] H.L. Fei, J.C. Dong, M.J. Arellano-Jiménez, G.L. Ye, N.D. Kim, E.L.G. Samuel, Z.W. Peng, Z. Zhu, F. Qin, J.M. Bao, M.J. Yacaman, P.M. Ajayan, D.L. Chen, J.M. Tour, Nat. Chem. 6 (2015) 8668.
[12] P.F. Zhang, Y.T. Gong, H.R. Li, Z.R. Chen, Y. Wang, Nat. Commun. 4 (2013) 1593.
[13] Y. Huan, H. Cheng, H. Yi, Y. Lin, T. Yao, C.L. Wang, J.J. Li, S.Q. Wei, J.L. Lu, J. Am. Chem. Soc. 137 (2015) 10484–10487.
[14] S.H. Sun, G.X. Zhang, N. Gauquelin, N. Chen, J.G. Zhou, S.L. Yang, W.F. Chen, X.B. Meng, D.S. Geng, M.N. Banis, R.Y. Li, S.Y. Ye, S. Knights, G.A. Botton, T.K. Sham, X.L. Sun, Sci. Rep. 3 (2013) 1775.
[15] M. Kaukonen, R.M. Nieminen, S. Pöykkö, A.P. Seitsonen, Phys. Rev. Lett. 83 (1999) 5346–5349.
[16] J.P. Perdew, K. Burke, M. Ernzerhof, Phys. Rev. Lett. 77 (1996) 3865–3868.
[17] W.H. Press, S.A. Teukolsky, W.T. Vetterling, B.P. Flannery, Numerical Recipes in C, Citeseer, (1996).
[18] H. Ibach, J.E. Rowe, Surf. Sci. 43 (1974) 481–492.
[19] Q. Guo, C.B. Xu, Z.F. Ren, W.S. Yang, Z.B. Ma, D.X. Dai, H.J. Fan, T.K. Minton, X.M. Yang, J. Am. Chem. Soc. 134 (2012) 13366–13373.
[20] C. Riedl, C. Coletti, T. Iwasaki, A.A. Zakharov, U. Starke, Phys. Rev. Lett. 103 (2009) 246804.
[21] J. VandeVondele, M. Krackb, F. Mohamedb, M. Parrinellob, T. Chassaingc, J. Hutterc, Comput. Phys. Commun. 167 (2005) 103–128.
[22] J. VandeVondele, J. Hutter, J. Chemi. Phys. 127 (2007) 114105.
[23] S. Goedecker, M. Teter, J. Hutter, Phys. Rev. B 54 (1996) 1703–1710.
[24] D.A. Drabold, P.A. Fedders, P. Stumm, Phys. Rev. B 49 (1994) 16415–16422.
[25] G. Galli, R.M. Martin, R. Car, M. Parrinello, Phys. Rev. Lett. 62 (1989) 555–558.
[26] W. Stöber, A. Fink, E. Bohn, J. Colloid Interface Sci. 26 (1968) 62–69.
[27] W.S. Hummers Jr., R.E. Offeman, J. Am. Chem. Soc. 80 (1958) 1339.
[28] J.S. Lee, K.H. You, C.B. Park, Adv. Mater. 24 (2012) 1084–1088.
[29] X.W. Lou, C.M. Li, L.A. Archer, Adv. Mater. 21 (2009) 2536–2539.
[30] M. Kaukonen, R.M. Nieminen, S. Pöykkö, A.P. Seitsonen, Phys. Rev. Lett. 83 (1999) 5346–5349.
[31] G. Vilé, D. Albani, M. Nachtegaal, Z. Chen, D. Dontsova, M. Antonietti, N. López, J. Pérez-Ramírez, Angew. Chem. Int. Ed. 54 (2015) 11265–11269.
[32] X.M. Chen, G.H. Wu, J.M. Chen, X. Chen, Z.X. Xie, X.R. Wang, J. Am. Chem. Soc. 133 (2011) 3693–3695.
[33] H.C. Choi, M. Shim, S. Bangsaruntip, H.J. Dai, J. Am. Chem. Soc. 124 (2002) 9058–9059.
[34] X. Li, J. Zhang, X.H. Zhao, Y.Y. Zhao, F. Li, T.H. Li, D.J. Wang, Nanoscale 6 (2014) 6473–6477.
[35] C.L. Su, R. Tandiana, J. Balapanuru, W. Tang, K. Pareek, C.T. Nai, T. Hayashi, K.P. Loh, J. Am. Chem. Soc. 137 (2015) 685–690.
[36] A.C. Ferrari, J.C. Meyer, V. Scardaci, C. Casiraghi, M. Lazzeri, F. Mauri, S. Piscanec, D. Jiang, K.S. Novoselov, S. Roth, A.K. Geim, Phy. Rev. Lett. 97 (2006) 187401–1874014.
[37] X.H. Li, X. Wang, M. Antonietti, Chem. Sci 3 (2012) 2170–2174.
[38] J.W. Xia, Y.S. Fu, G.Y. He, X.Q. Sun, X. Wang, Appl. Catal. B 200 (2017) 39–46.
[39] S. Back, J.H. Lim, N.Y. Kim, Y.H. Kim, Y.S. Jung, Chem. Sci. 8 (2017) 1090–1096.
[40] X.M. Gu, W. Qi, X.Z. Xu, Z.H. Sun, L.Y. Zhang, W. Liu, X.L. Pan, D.S. Su, Nanoscale 6 (2014) 6609–6616.
[41] Z. Chen, Z.M. Cui, F. Niu, L. Jiang, W.G. Song, Chem. Commun 46 (2010) 6524–6526.
[42] T. Zeng, X.L. Zhang, S.H. Wang, H.Y. Niu, Y.Q. Cai, Environ. Sci. Technol. 49 (2015) 2350–2357.
[43] X.L. Pan, Z.L. Fan, W. Chen, Y.J. Ding, H.Y. Luo, X.H. Bao, Nat. Mater. 6 (2007) 507.